Likely frost events at Gale crater: Analysis from MSL/REMS measurements

G. M. Martínez, E. Fischer, N. O. Rennó, E. Sebastián, O. Kemppinen, N. Bridges, C. S. Borlina, P. -Y. Meslin, M. Genzer, A. -H. Harri, et al.

Icarus 280 (2016) 93–102

Contents lists available at ScienceDirect

Icarus

journal homepage: www.elsevier.com/locate/icarus

Likely frost events at Gale crater: Analysis from MSL/REMS measurements

G.M. Martínez[a,*], E. Fischer[a], N.O. Rennó[a], E. Sebastián[b], O. Kemppinen[c], N. Bridges[d], C.S. Borlina[a], P.-Y. Meslin[e], M. Genzer[c], A.-H. Harri[c], A. Vicente-Retortillo[f], M. Ramos[g], M. de la Torre Juárez[h], F. Gómez[b], J. Gómez-Elvira[b], the REMS Team

[a] Department of Climate and Space Sciences and Engineering, University of Michigan, Ann Arbor, MI, USA
[b] Centro de Astrobiología, Torrejón de Ardoz, Madrid, Spain
[c] Finnish Meteorological Institute, Helsinki, Finland
[d] Johns Hopkins University Applied Physics Laboratory, Laurel, MD 20723, USA
[e] Université de Toulouse, UPS-OMP, IRAP, 31028 Toulouse, France
[f] Departamento de Física de la Tierra, Astronomía y Astrofísica II, Facultad de Ciencias Físicas, Universidad Complutense, Madrid, Spain
[g] Departamento de Física, Universidad de Alcalá de Henares, Madrid, Spain
[h] Jet Propulsion Laboratory, California Institute of Technology, 4800 Oak Grove Drive, Pasadena, CA 91109, USA

ARTICLE INFO

Article history:
Received 12 July 2015
Revised 17 November 2015
Accepted 2 December 2015
Available online 19 December 2015

Keywords:
Mars, surface
Mars, atmosphere
Ices

ABSTRACT

We provide indirect evidence for the formation of frost at the surface of Gale crater by analyzing the highest confidence data from simultaneous measurements of relative humidity and ground temperature during the first 1000 sols of the Mars Science Laboratory (MSL) mission. We find that except for sol 44, frost events could have occurred only between sols 400 and 710, corresponding to the most humid and coldest time of the year (from early fall to late winter). In particular, measurements at Dingo Gap during sols 529–535, at an unnamed place during sols 554–560, at Kimberley during sols 609–617 and at an unnamed place during sols 673–676 showed the largest likelihood of the occurrence of frost events. At these four locations, the terrain is composed of fine-grained and loosely packed material with thermal inertia values of ~200 SI units, much lower than the 365 ± 50 SI units value found at the landing ellipse. This is important because terrains with exceptionally low thermal inertia favor the formation of frost by lowering minimum daily ground temperatures. An order-of-magnitude calculation to determine the thickness of the frost layer at these four locations results in values of tenths of μm, while the precipitable water content is a few pr-μm. Therefore, surface frost events can have important implications for the local water cycle at Gale crater. In addition, frost is the most likely type of water that can be temporarily found in bulk amounts on the surface of Mars at low latitudes and therefore can cause weathering, influencing the geology of Gale crater.

1. Introduction

Frost forms on a surface if its temperature drops below the frost point of the surrounding air. At low latitudes, frost is the most likely type of water that can be found temporarily in bulk quantities on the surface of Mars. Since at low latitudes the near-surface environment is relatively warm and dry (Mellon et al., 2004), ice is unlikely to be deposited on the surface by snowfall or fog [as opposed to polar latitudes, where both are common (Whiteway et al., 2009)]. Similarly, ice is unlikely to be present in the first meter of the subsurface at low latitudes because it would be thermodynamically unstable (Schorghofer and Aharonson, 2005; Mitrofanov et al., 2014). However, we show that measurements by the Rover Environmental Monitoring Station (REMS) aboard the Curiosity rover (Gómez-Elvira et al., 2014) suggest that frost could form temporarily on the surface of Gale crater (4.5°S). In particular, we show that the ground temperature at Gale crater likely dropped below the frost point on several sols during the Mars Science Laboratory (MSL) mission.

Surface frost events can have important implications for the local water cycle at Gale crater (Martín-Torres et al., 2015). Loss of atmospheric water vapor by deposition on the surface and subsequent sublimation can cause significant variability in the

* Corresponding author.

http://dx.doi.org/10.1016/j.icarus.2015.12.004

atmospheric water vapor content (Moores et al., 2011) as well as have an impact on the interaction between the atmosphere and the regolith (Jakosky et al., 1997). In addition, the transport of frost within soils by water vapor diffusion also affects the geochemistry and geologic nature of the surface and near sub-surface. Chlorine and sulfur mobilized by vapor diffusion can occur even in equatorial regions (Jakosky and Christensen, 1986). These chemical compounds are associated with cohesive or hardened soil surfaces (Clark et al., 1982; Rieder et al., 1997, 2004) that, if extensive enough, may produce the high thermal inertia duricrusts inferred from orbital measurements (Jakosky and Christensen, 1986). Many ripples and megaripples on Mars consist of fine grained interior deposits anchored in place by a carapace of coarse grains (Sullivan et al., 2005, 2014; Sullivan and Zimbelman, 2015). Such a structure of fine grains, with high surface area to volume ratio, is a potential zone where vapor can be concentrated, along with associated salts. Indeed, the structure of the Dingo Gap megaripple has this character and, as we show, this is the area where the most likely frost events were identified.

Frost formation could also explain the ubiquitous hydration signatures observed from orbit by the OMEGA instrument (Audouard et al., 2014). Frost may for instance be responsible for the formation of the hydrated amorphous component inferred from Curiosity measurements of the martian soil (Leshin et al., 2013; Meslin et al., 2013).

Prior to the MSL mission, the formation of surface frost has been confirmed at polar and mid latitudes. At the Phoenix landing site (68.22°N), nighttime frost was detected by the Robotic Arm Camera from sol 80 (early summer, $L_s \sim 113°$) until the end of the mission on sol 151 (late summer, $L_s \sim 149°$) (Smith et al., 2009). The Phoenix observation provided ground-truth to the detection of a ~20 μm thick layer of frost by satellite measurements (Cull et al., 2010). This is important because laboratory experiments conducted at polar environmental conditions show that liquid brine can form minutes after the ground exceeds the eutectic temperature of salts in contact with water ice (Fischer et al., 2014). Similarly, at the Viking Lander 2 site (47.7°N), a thin layer of frost was observed on the ground for about 250 sols, from late winter until spring in the first year of the mission. At this location, frost formed at night and persisted throughout the day, with an estimated maximum thickness ranging from ~0.5 mm to a few millimeters (Jones et al., 1979; Wall, 1981).

At low latitudes, where the surface is warmer and near-surface water vapor pressures are lower (Mellon et al., 2004), ground frost events have not been observed by landers or rovers yet. However, there is evidence that frost events occur at low latitudes. Visual evidence for the formation of frost has been found on the deck and calibration target of the MER-B (1.95°S) on sol 257 (late southern winter) (Landis, 2007; Möhlmann, 2008). At the Viking Lander 1 site (28.3°N), Pathfinder site (19.3°N) and MER-A site (14.5°S) frost has not been observed, but numerical simulations indicate that frost is likely to form at these locations at night (Savijärvi, 1995, 1999, 2012). At Gale crater, numerical simulations suggest that frost could have formed during the night on the first sols of the mission, but that it would have been difficult to detect it because the frost would be extremely thin (Harri et al., 2014a). More recent numerical simulations suggest that nighttime frost could have formed at Gale crater during sols 15–17 if the water column abundances were higher than 10 pr-μm, but that more likely values of ~5 pr-μm would have prevented the formation of frost (Savijärvi et al., 2015).

MSL is equipped with instruments (Grotzinger et al., 2012) capable of detecting frost. These instruments include REMS (Gómez-Elvira et al., 2012), the Chemistry and Camera instrument (ChemCam) (Maurice et al., 2012), the Dynamic Albedo of Neutrons (DAN) instrument (Mitrofanov et al., 2012) and the Mast Camera (Mastcam). In this article, we use REMS measurements to show evidence that frost forms at Gale crater. In addition to REMS, ChemCam can provide remote observations of surface coatings such as frost by analyzing the evaporates from pulsed laser radiation pointed at the surface, while DAN could detect frost by measuring changes in the hydrogen content of the regolith down to about one meter below the surface. Hydrogen can exist as part of the chemical structure of hydrated minerals (chemically bounded water), as part of water adsorbed in the regolith (physically bounded water or just adsorbed water) and as part of water ice in the regolith (Mitrofanov et al., 2014; Martínez and Renno, 2013). Finally, frost could be detected using Mastcam color images with a resolution as high as 150 μm/pixel. We shown in Section 5.3 that ChemCam, DAN and Mastcam have not detected frost at Gale crater yet.

Section 2 describes the REMS data used in this article. Section 3 explains the methodology developed to detect surface frost events. Section 4 shows the results, including a detailed analysis of the environmental conditions when the surface frost events are most likely to occur, as well as calculations of the thickness of the frost formed on these sols. Section 5 discusses the results. Finally, Section 6 contains the summary and main conclusions of the article.

2. REMS Relative Humidity Sensor and Ground Temperature Sensor measurements

REMS was developed to assess the environmental conditions along Curiosity's traverse at Gale crater by measuring atmospheric pressure (Harri et al., 2014b), atmospheric relative humidity (Harri et al., 2014a), ground and atmospheric temperatures (Martínez et al., 2014; Hamilton et al., 2014), UV radiation fluxes and horizontal wind speeds. This article focuses on the analysis of REMS ground temperature (T_g) and atmospheric relative humidity (RH) measurements.

The REMS Relative Humidity Sensor (RHS), designed and built by the Finnish Meteorological Institute and mounted on the REMS boom 2, consists of three polymeric sensors that measure the relative humidity at 1.6 m height ($RH1.6m$). The RHS contains a sensor to measure the temperature (T_{RH}) of the air entering the Relative Humidity Sensor (see Harri et al., 2014a for details). T_{RH} is estimated to deviate from the ambient temperatures by less than 1 K (Savijärvi et al., 2015).

Nominally, the RHS operates at 1 Hz during the first five minutes of each hour, with an additional hour of continuous measurements at 1 Hz on each sol (Gómez-Elvira et al., 2014). The RHS has recently been recalibrated (June 2015), providing relative humidity values slightly lower than those in the previous calibration (December 2014). In this article, we only use RHS data obtained with the latest recalibration parameters and taken during the first three seconds of measurements after the sensor has been turned off for more than 30 min. This is done to avoid the artificially low values of relative humidity due to the heating of the sensor by the REMS control electronics. During the first three seconds the measurement stays stable. The average of the $RH1.6m$ and T_{RH} values of the measurements during these three seconds is then calculated. Our data analysis strategy results in 24 hourly values of $RH1.6m$ and T_{RH} per sol (hereinafter called $\overline{RH1.6m}$ and $\overline{T}_{RH}$).

Fig. 1 shows the maximum $\overline{RH1.6m}$ value per sol for the first 1000 sols of the MSL mission (one martian year = 669 sols). The highest annual values occurred around early winter, with a maximum of about 70% on sol 551 ($L_s \sim 93°$). The lowest annual values occurred around late spring and early summer, when the maximum $\overline{RH1.6m}$ stayed below 10%. Contrary to the Phoenix landing site (Whiteway et al., 2009), near-surface fog did not form at Gale crater because the $\overline{RH1.6m}$ values never reached 100%. However, the nighttime and early morning ground temperature can be about

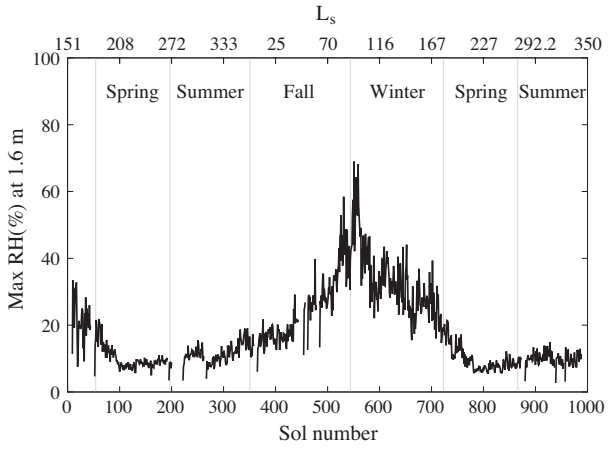

Fig. 1. Evolution of the maximum relative humidity at 1.6 m per sol at Gale during the first 1000 sols as measured by the REMS/RHS instrument. Here we only show *RH* measurements with the highest confidence obtained during the first three seconds after the sensor has been turned off for more than 30 min to avoid spurious effects due to heating.

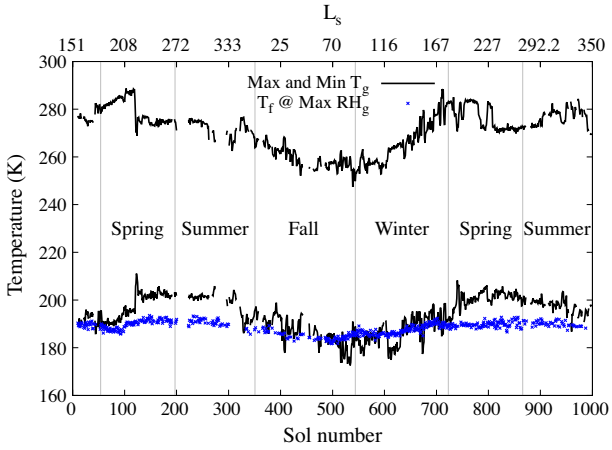

Fig. 2. Evolution of the maximum and minimum ground temperatures (black curves) at Gale during the first 1000 sols as measured by the REMS/GTS instrument. The frost point derived from the REMS/RHS instrument when the relative humidity at the ground is the highest is shown in blue. The ground temperature falls below the frost point on several sols during fall and winter, and on a few sols during summer and spring, indicating that surface frost events at Gale are possible. (For interpretation of the references to color in this figure legend, the reader is referred to the web version of this article.)

12 K colder than that at 1.6 m above the surface, allowing the ground to reach the frost point temperature on some sols as shown in Section 3. The reader is referred to Section 5.1 for a comprehensive analysis of Fig. 1 with respect to the broader environmental context at Gale crater.

The REMS Ground Temperature Sensor (GTS), designed at Centro de Astrobiología in Spain, is located at the base of boom 1 at about 1.6 m above the ground. The sensor consists of three thermopiles inside a housing designed to reduce the temperature gradients in the system. Surface brightness temperatures are derived from measurements in the bandwidths 8–14, 15.5–19, and 14.5–15.5 μm, which were chosen to minimize reflected solar irradiance (<0.5%). The GTS points toward 120° azimuth (with 0° being the rover forward-looking direction, counting clockwise), and −26° declination (downward from the plane of the rover deck), with a field of view (FOV) of 60° horizontally and 40° vertically. This FOV covers a ground area of about 100 m^2, assuming zero roll and pitch angles over flat terrain (see Sebastián et al., 2010 for more details).

The GTS nominally makes 1 Hz measurements during the first five minutes of each hour. In addition, continuous measurements at 1 Hz are frequently made in one-hour blocks per sol (Gómez-Elvira et al., 2014). In this study we only use GTS measurements with the highest confidence level (ASIC power supply in range, highest recalibration quality and no shadows in the GTS FOV) to minimize errors. By averaging these measurements over a 5-min interval, noise is reduced and high quality hourly ($\overline{T_g}$) data is obtained.

Fig. 2 (black curves) shows the maximum and the minimum $\overline{T_g}$ per sol for the first 1000 sols. The lowest ground temperatures at Gale occurred during late fall and early winter, with the annual minimum temperature (~173 K) occurring at Dingo Gap on sol 534 ($L_s = 85°$). On the other extreme, the highest ground temperatures occurred during late winter and early spring, with the annual maximum temperature (~289 K) occurring on sols 103 and 711 ($L_s = 210°$ and 174°).

The frost point temperature $\overline{T_f}$ at the time when the relative humidity at the ground ($\overline{RH_g}$) is the highest is shown in blue in Fig. 2. The ground temperature is lower than $\overline{T_f}$ on several sols during fall and winter and on a few sols during summer and spring, indicating that surface frost events at Gale are possible. The frost point temperature has been calculated using the water vapor pressure at 1.6 m as

$$\overline{e1.6m} = \overline{RH1.6m} \times e_s(\overline{T_{RH}}), \quad (1)$$

where e_s is the saturation vapor pressure over ice (Savijärvi et al., 2015). Note that in Fig. 2 we compare ground temperatures with frost point temperatures calculated using values at 1.6 m [Eq. (1)]. This is a valid assumption to search for surface frost events when the water vapor pressure is nearly constant in the first 1.6 m because in this case the frost point temperature at the ground and at 1.6 m are similar.

3. Identification of frost events

We identify surface frost events along Curiosity's traverse by analyzing simultaneous RHS and GTS measurements with the highest confidence made during the first 1000 sols of the mission. We use two independent conditions on GTS and RHS measurements to determine the sol number and the local mean solar time when a surface frost event is likely to have occurred.

First, we impose that for any given pair of simultaneous $\overline{T_g}$,$\overline{T_f}$ values, the ground temperature must fall below the frost point ($\overline{T_g} < \overline{T_f}$). This is a sufficient condition for frost to form. In order to quantify the likelihood that this condition is met for pairs of $\overline{T_g}$,$\overline{T_f}$ values, we obtain the value of an auxiliary parameter k that represents the certainty with which the ground temperature is below the frost point:

$$\overline{T_g} + k\sigma_{Tg} < \overline{T_f} - k\Delta T_f, \quad (2)$$

where σ_{Tg} is the standard deviation of the $\overline{T_g}$ measurements, and ΔT_f is the uncertainty in the calculation of $\overline{T_f}$. Assuming that $\overline{T_g}$ and $\overline{T_f}$ follow a Gaussian distribution, a value of $k = 3$ would imply a probability > 99.7% that a frost event occurred. The calculation of σ_{Tg} and ΔT_f is explained in Appendix A.

Fig. 3 shows the values of k that satisfy Eq. (2). We find that except for sol 44, frost events could have occurred only between sols 400 and 710, corresponding to the most humid and coldest time of the year (from early fall to late winter; see Figs. 1 and 2). Between sols 1 and 400, and sols 710 and 1000, corresponding to the lowest *RH* and warmest period of the year (spring and

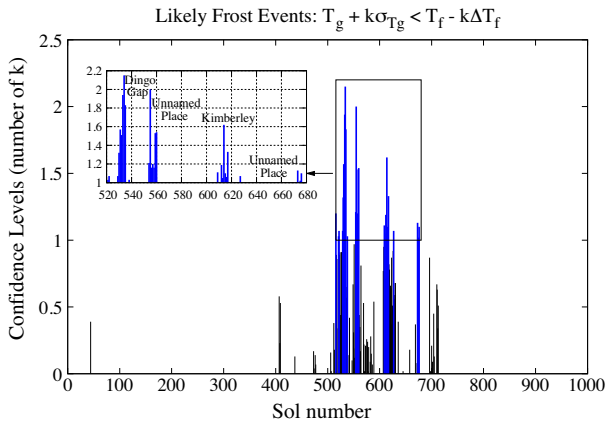

Fig. 3. Number k of standard deviations in ground temperature (σ_{Tg}) and uncertainty in the frost point (ΔT_f) for which the relation $T_g + k\sigma_{Tg} < T_f - k\Delta T_f$ is met. Note that a value of $k = 3$ would imply a probability > 99.7% for a frost event if T_g and T_f strictly followed a Gaussian distribution. Four temporal windows colored in blue show the largest likelihood ($k \geqslant 1$) in surface frost events: Dingo Gap on sols 529–535, an unnamed place on sols 554–560, Kimberley on sols 609–617 and an unnamed place on sols 673–676. These four temporal windows correspond to the most humid and coldest time of the year (from early fall to late winter; Figs. 1 and 2). (For interpretation of the references to color in this figure legend, the reader is referred to the web version of this article.)

summer), the ground temperature was always above the frost point temperature.

The most likely frost events ($k \geqslant 1$) within the first 1000 sols occurred between sols 520 and 680. This period is highlighted in Fig. 3 insert. In particular, four time periods show the largest likelihood of frost events: sols 529–535 at Dingo Gap, sols 554–560 at an unnamed place, sols 609–617 at Kimberley, and sols 673–676 also at an unnamed place.

Following surface frost formation, a decrease in near-surface water vapor pressure is expected because water vapor in direct contact with the ground is removed by direct deposition onto the surface (Moores et al., 2011; Savijärvi and Määttänen, 2010). Therefore, we search for decreases in water vapor pressure as an independent indication of frost events. We find that on 93% of the sols shown in the insert of Fig. 3 ($k \geqslant 1$), a decrease in water vapor pressure occurs during the period in which a frost event is identified with the largest confidence. A similar decrease in water vapor pressure is found on 82% of the sols with $k < 1$. However, on sols where frost events are not predicted, a decrease in water vapor between 4 and 6 am (typical frost event period) only occurs on 54% of these sols. This analysis supports the identification of frost events using Eq. (2) because it shows a strong correlation between the confidence of a frost event (value of k) and the simultaneous decrease in water vapor pressure. However, it also indicates that a decrease in water vapor pressure is not unambiguously indicative of frost formation, but simply consistent with it. In fact, phenomena like adsorption of water vapor by the ground may also cause a decrease in water vapor pressure.

The terrain in the field of view of the GTS during the sols when frost events most likely occurred is shown in Fig. 4. The GTS footprint in Fig. 4a covers the base of the Dingo Gap megaripple, a surface that consists of a coarse carapace overlying a fine-grained interior (Sullivan et al., 2014). The unnamed location in Fig. 4b is ~475 m WSW from Dingo Gap, within a valley. The GTS footprint covers rocks and fines that, geologically, seem similar to other areas of the traverse. This is unlike the Dingo Gap megaripple which, being the largest such feature visited by any Mars rover, is far more unique. The other two locations at Kimberley on sol 609 and at an unnamed place on sol 674 are shown in Fig. 4c and d, with the terrain showing similar features to that of the Dingo Gap megaripple.

4. Results: Characterization of the most likely frost events

We select sols 531, 557, 612 and 676 to analyze the environmental conditions that most likely resulted in the formation of frost. These sols are representative of the four locations because the environmental conditions at each location stayed comparably stable. Additionally, we show an order-of-magnitude estimate of the thickness of the frost layer that likely formed at these locations.

The diurnal evolution of $\overline{T_g}$ and $\overline{T_f}$ on sols 531, 557, 612 and 676 is shown in Fig. 5. The ground temperature was below the frost point temperature with a confidence of $k \geqslant 1$ [see Eq. (2)] between 4 and 6 am LMST on sol 531, between 4 and 5 am on sols 557 and 612, and only at 5 am on sol 676, indicating that frost is most likely to form during these time periods.

After sunrise at around 6 am on all these sols, the ground temperature increased rapidly, exceeding the frost point shortly after 6 am, and then staying well above it throughout the day. Therefore, any frost formed at night would have quickly sublimated during the day. This is important because ChemCam performed soil analyses on these sols only in the afternoon.

Here, we provide an order-of-magnitude estimate of the thickness of the frost layer predicted to have formed on sols 529–535 at Dingo Gap, sols 554–560 at an unnamed place, sols 609–617 at Kimberley, and sols 673–676 also at an unnamed place. Following frost formation, a decrease in water vapor pressure is expected because the water vapor would be removed by direct deposition onto the surface. As shown in Section 2, on 93% of the sols when a frost event is identified with the largest confidence between 4 and 6 am, a simultaneous decrease in water vapor pressure occurs within the same time period. However, on sols where frost events are not predicted, a decrease in water vapor between 4 and 6 am only occurs on 54% of these sols. Given the strong correlation between the confidence of a frost event (value of k) and the simultaneous decrease in water vapor pressure, we make the assumption that the decrease in water vapor pressure that occurs simultaneous to the largest confidence frost events can be attributed to the formation of frost.

Fig. 6 shows the diurnal evolution of $\overline{e1.6m}$ (blue crosses) along with its uncertainty (red crosses) on sols 531, 557, 612 and 676. Since frost events starting at 4 am on sols 531, 557 and 612, and at 5 am on sol 676 have been identified with the highest confidence (Fig. 5), we attribute the subsequent decrease in $\overline{e1.6m}$ while the ground temperature remains below the frost point to the formation of frost at the surface. These time periods are highlighted by the gray shaded area in Fig. 6.

By making this approximation, we can estimate the thickness (h) of the frost layer using the decrease in water vapor pressure highlighted in Fig. 6. In this case, our estimate represents a lower bound of the thickness because we calculate the thickness of the frost layer only during the short time period in which the surface temperature is lower than the frost point by a margin greater than the sum of the one-standard-deviation uncertainties in each measurement ($k \geqslant 1$). This is a conservative criterion because frost could also have formed when this margin is lower ($k < 1$), as for instance on sol 531 between 0 and 2 am and between 10 and 11 pm (Fig. 5a). However, the relative error in water vapor values outside the period between 4 and 6 am ($k \geqslant 1$) can exceed 100%, even during the sols when the frost events are most likely to occur. For instance, Fig. 6a shows that on sol 531 the relative error in the water vapor pressure is above 100% between 0 and 2 LMST and between 22 and 23 LMST (when the ground temperature is lower than the frost point, but with a certainty $k < 1$, Fig. 5a).

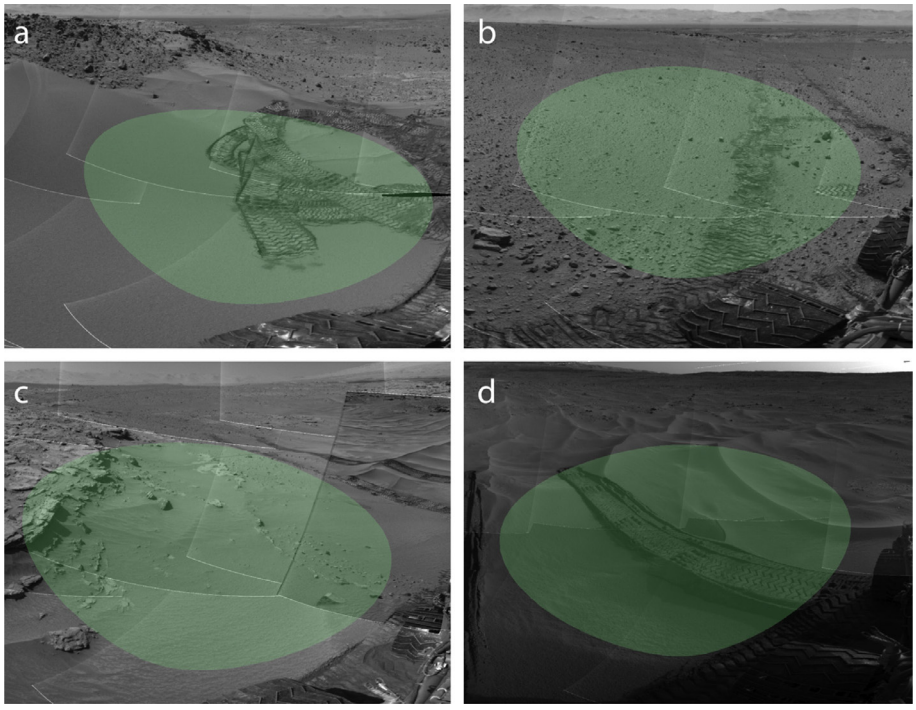

Fig. 4. Navcam mosaics showing the terrain monitored by the REMS/GTS in green on sol 533 at Dingo Gap megaripple (a), sol 559 at an unnamed place (b), sol 609 at Kimberley (c) and sol 674 at an unnamed place (d). The most likely frost events during the first 1000 sols of the MSL mission occurred on the terrain shown above. The GTS footprint in (a), (b) and (d) covers a terrain consisting of a coarse carapace overlying a fine grained interior, while in (b) the GTS footprint covers rocks and fines that, geologically, seem similar to other areas of the traverse. (For interpretation of the references to color in this figure legend, the reader is referred to the web version of this article.)

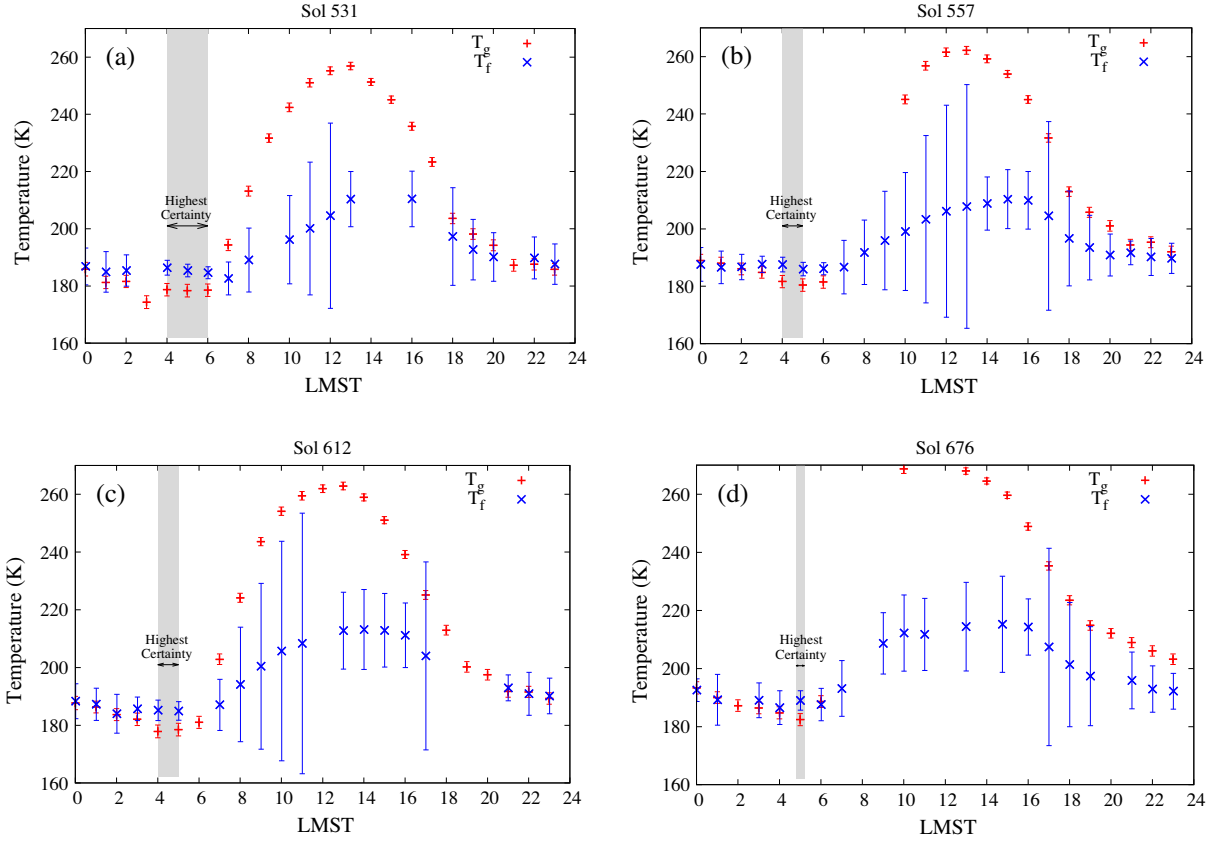

Fig. 5. Diurnal evolution of ground temperature (red curve) and frost point (blue curve) on sols 531 (a), 557 (b), 612 (c) and 676 (d). The times during which the ground temperature falls below the frost point with the highest confidence are represented by the gray shaded area, indicating that frost is most likely to form during these time periods. (For interpretation of the references to color in this figure legend, the reader is referred to the web version of this article.)

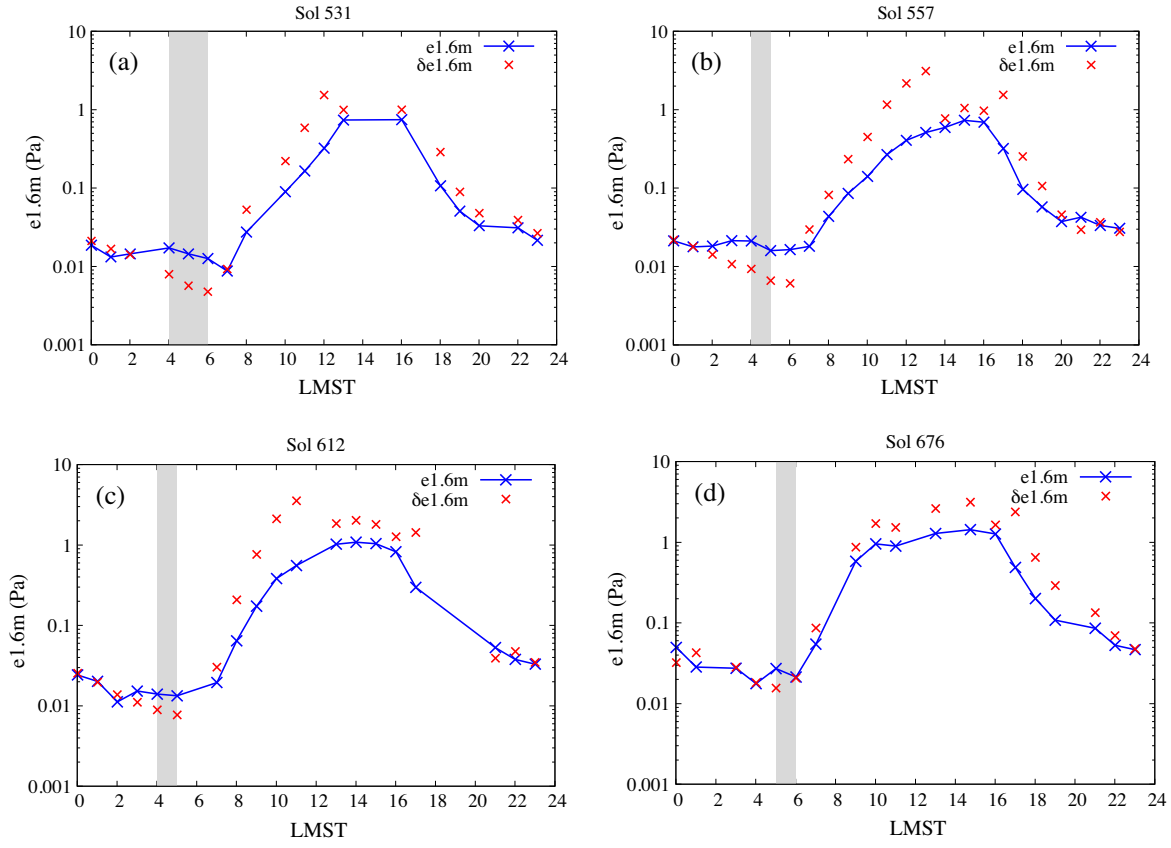

Fig. 6. Diurnal evolution of water vapor pressure at 1.6 m (e1.6 m, blue curve) and its uncertainty (δe, red crosses) on the same sols as in Fig. 5. The decrease in water vapor highlighted by the gray stripe on each sol is consistent with frost formation because during these periods, the ground temperature was below the frost point temperature with the highest confidence (Fig. 5). With except for the time periods highlighted in gray, the uncertainty in $\overline{e1.6m}$ is significant, particularly in the daytime when the relative error is higher than 100%. Therefore, daytime values of water vapor pressure are unreliable. The reader is referred to the appendix for details on the calculation of $\overline{e1.6m}$ uncertainties. (For interpretation of the references to color in this figure legend, the reader is referred to the web version of this article.)

Consequently, we provide estimations of the frost layer thickness formed only between 4 and 6 am. This corresponds to a lower-bound value.

The precipitable water content (*PWC*) is defined as the thickness of the liquid layer formed if all the water vapor content in the atmospheric column was precipitated onto the surface. It can be calculated as

$$PWC = \int_0^\infty q(z)\rho(z)dz, \tag{3}$$

where q stands for the specific humidity (mass of water vapor per mass of air) and ρ for the density of the air. Assuming that water vapor is uniformly mixed in the vertical (Harri et al., 2014a) before a surface frost event starts, Eq. (3) can be rewritten as

$$PWC = q_0 \int_0^\infty \rho(z)dz = q_0 \int_0^\infty \rho_0 e^{-z/H}dz = \frac{H}{R_v}\frac{e_0}{T_0}, \tag{4}$$

where q_0 and T_0 are the specific humidity and temperature at the surface, $R_v = 461\ \mathrm{kg^{-1}\ K^{-1}}$ is the specific gas constant of water vapor, and $H = 9.7$ km is the scale height at Gale for a near-surface temperature of 190 K (as measured by the air temperature sensor between 4 and 6 am during the sols shown in Figs. 5 and 6). Assuming that the decrease in water vapor pressure (Δe) highlighted in Fig. 6 is caused by frost formation on the surface, the thickness of the frost layer can be calculated from the decrease in the *PWC* as

$$h\ (\mu\mathrm{m}) = \frac{\rho_w}{\rho_i}\Delta PWC\ (\text{pr-}\mu\mathrm{m}) = \frac{\rho_w}{\rho_i}\frac{H}{R_v}\frac{1}{T_g}\Delta e, \tag{5}$$

where Eq. (4) has been used. Here, $\rho_i = 925\ \mathrm{kg/m^3}$ is the density of the ice at $T_g \approx 180$ K (see Fig. 5 between 4 and 6 am) and $\rho_w = 1000\ \mathrm{kg/m^3}$ is the density of the liquid water.

Fig. 7 shows the estimated thickness of the frost layer obtained from Eq. (5). Our calculations indicate values of h of ~0.7 μm

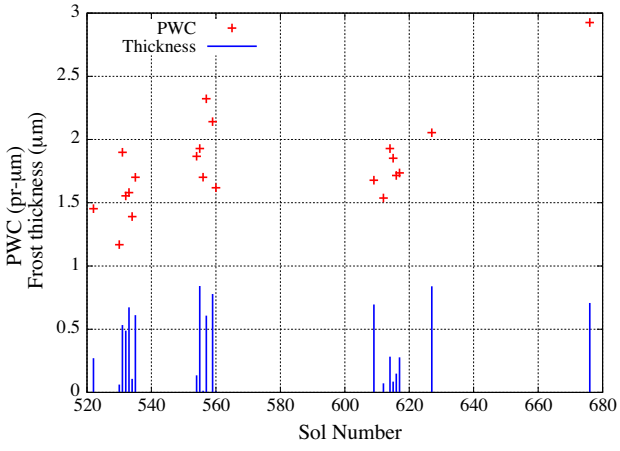

Fig. 7. Thickness of the frost layer (blue) and precipitable water content (red) obtained for the sols with the largest likelihood of occurrence of frost events at Gale. The thickness of the frost layer shows values of the order of tenths of μm, while the precipitable water content shows values of a few precipitable micrometers. (For interpretation of the references to color in this figure legend, the reader is referred to the web version of this article.)

at Dingo Gap between sols 529 and 535, of ~0.8 μm at the unnamed place between sols 554 and 560, of ~0.7 μm at Kimberly between sols 609 and 617, and of ~0.7 μm at the unnamed place on sol 676. Fig. 7 also shows nighttime *PWC* values calculated from Eq. (4), with e_0 the water vapor pressure at the time at which the frost events most likely started (4 am on sols 531, 557 and 612 and 5 am on sol 676; Fig. 6). *PWC* values range from 1.2 pr-μm at Dingo Gap, to 2.9 pr-μm on sol 676. These results suggest that: (i) either a considerable portion of the *PWC* was deposited on the surface in a few hours, or that (ii) the terrain at these four locations was acting as a cold trap, bringing in moist air from the surroundings, or that (iii) the two previous mechanisms were acting together. This is discussed in more detail in Section 5.3.

Finally, we note that the decrease in water vapor pressure highlighted in Fig. 6 is slightly larger than the uncertainty in $\overline{e1.6m}$, which still allows the use of Δe in Eq. (5) to calculate h. However, they are still of the same order of magnitude (10^{-3} Pa; see Fig. 6 between 4 and 6 am), and thus h values represent a first-order approximation of the thickness of the frost layer. We also note that a change of $\Delta e \approx 0.007$ Pa, as that occured on sol 531 between 4 and 6 am, would have caused an increment of ground temperature of only about ~0.01 K, as follows from $\Delta T_g = (L_{sub}\varepsilon/Pc_p)\ \Delta e$, where $L_{sub} \approx 2.8 \times 10^6$ J kg^{-1} is the latent heat of sublimation, $c_p = 736$ J kg^{-1} K^{-1} is the heat capacity of the air at constant pressure, and $\varepsilon = 0.41$ is the ratio of gas constants for dry air to that for water vapor. Such a tiny variation in the ground temperature is beyond the resolution of the GTS, and therefore changes of ground temperature due to frost formation are not detectable.

5. Discussion

In this section, we first discuss the environmental conditions and the type of terrain that likely led to the formation of surface frost at Gale. Then, we discuss the daily variability of near-surface water content. Finally we discuss the impact of frost formation on changes in the atmospheric water content.

5.1. Frost events in the climatological context at Gale

The relative humidity [$RH = e/e_s(T)$] depends on atmospheric water vapor content and temperature. We show that at Curiosity's landing site, the seasonal evolution of the relative humidity is mainly controlled by temperature. The maximum diurnal value of the relative humidity shown for the first 1000 sols in Fig. 1 follows the minimum diurnal value of the ground temperature shown by the lower black curve in Fig. 2. This is because on every sol, the maximum diurnal value of $\overline{RH1.6m}$ generally occurs at the same time as the minimum diurnal value of $\overline{T_g}$. Therefore, in early winter, when the diurnal minimum temperatures are the lowest of the year, the relative humidity shows the highest annual values. Similarly, in spring and summer, when the diurnal minimum temperatures are the highest of the year, the relative humidity shows the lowest annual values on both years.

Interestingly, the seasonal evolution of the relative humidity appears to be anti-correlated with the seasonal evolution of near-surface water vapor pressure shown in Fig. 8. On one hand, the lowest annual values of $\overline{e1.6m}$ occur in late fall and early winter, when $\overline{RH1.6m}$ is the highest (Fig. 1). On the other hand, the highest annual values of $\overline{e1.6m}$ occur in late spring, early summer, and late winter, when $\overline{RH1.6m}$ is the lowest.

The sol-to-sol variability in $\overline{e1.6m}$ shown in Fig. 8 is larger around the annual maximum than around the annual minimum. This variability might be related to the uncertainty in $\overline{e1.6m}$ measurements rather than to actual variations in $\overline{e1.6m}$. Diurnally, the most accurate value of water vapor pressure corresponds to the time of the day when the relative humidity is the highest

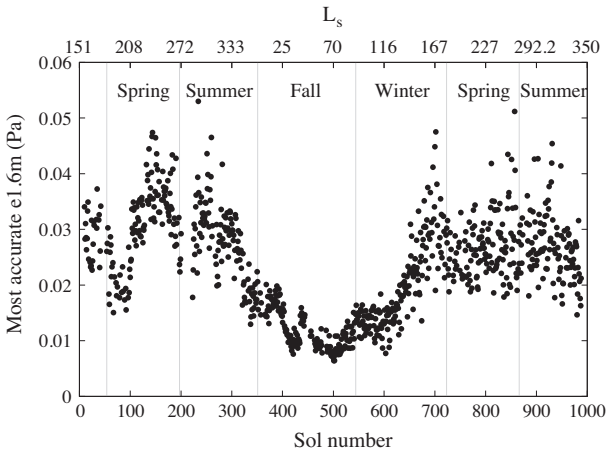

Fig. 8. Evolution of the water vapor pressure at 1.6 m at Gale during the first 1000 sols. We only show the most accurate $\overline{e1.6m}$ value per sol, which corresponds to the time of the day when $\overline{RH1.6m}$ is the highest, usually between 4 and 6 am as shown in Fig. 6.

(between 4 and 6 am, as shown in Fig. 6). Annually, $\overline{RH1.6m}$ shows the highest values around late fall and early winter (Fig. 1). Therefore, $\overline{e1.6m}$ values around this time of the year present the highest accuracy and lowest day-to-day variability (Fig. 8). In contrast, $\overline{RH1.6m}$ shows the lowest annual values in spring and summer (Fig. 1). Therefore, $\overline{e1.6m}$ values around this time of the year present the lowest accuracy and largest day-to-day variability (Fig. 8).

We have shown that the most likely frost events occurred between sols 520 and 680 (Fig. 3) simply because this was the coldest time of the year (and therefore the most humid time of the year despite corresponding to an annual minimum in water vapor pressure). Next we show that the type of terrain also plays an important role in frost formation. We have used the methodology developed by Martínez et al. (2014) to calculate the thermal inertia (I) of the four terrains on which frost formed at Gale (Fig. 4), obtaining ~200 SI units for each of them. This value is exceptionally low compared to previous estimations of I in other places at Gale crater. Using REMS/GTS measurements, Martínez et al. (2014) obtained I values of ~450 SI units at Yellowknife Bay, and ~300 SI units at Rocknest. Also at Gale, but using Thermal Emission Spectrometer (TES) data with a horizontal resolution of ~10^7 m^2, Christensen et al. (2001) and Putzig et al. (2005) obtained I values ranging from 335 to 425 SI units, while Fergason et al. (2012) obtained I values of 365 ± 50 SI units at the landing ellipse using THEMIS data with a resolution of 10^4 m^2. Thus, the thermal inertia estimated for the terrain shown in Fig. 4 is exceptionally low. This is important because terrains with low values of I, consistent with fine-grained and loosely packed material, amplify the diurnal amplitude in ground temperature, producing lower daily minimum temperatures and thus facilitating frost formation.

At Gale, none of the instruments aboard MSL has yet detected frost directly. ChemCam has been used in four different campaigns designed to search for frost between 04:30 and 06:00 on sols 75, 290, 317 and 545. However, no signs of an elevated H signal were detected on any of these sols (Schröder et al., 2015). As shown in Sections 2 and 3, the ground temperature never dropped below the frost point on any of these sols, indicating that frost would not have been detected when the search was conducted. Additionally, since ice is not stable in the shallow subsurface at the latitude of Gale crater, and DAN is sensitive to the bulk shallow subsurface material, it is unlikely that DAN would have been able to detect

the weak signal of a frost layer that is only a few tenths of a micrometer thick (Fig. 7). Furthermore, DAN was not used to search for frost around sunrise, when frost events are most likely to occur. Finally, Mastcam has not been used to search for frost at the time that it is most likely to form.

Frost is most likely to form on megaripples (Fig. 4) with very low thermal inertia and therefore low daily minimum temperatures. Measurements and images taken between 4 and 6 am during late fall and early winter, when both the annual and daily temperatures are the lowest (Figs. 2 and 5) and the relative humidity is the highest (Fig. 1), have the highest probability of providing direct evidence of frost at the latitudes of Gale crater.

5.2. Daily variability of near-surface water content at Gale

Fig. 6 shows that over the course of the day, the most accurate water vapor pressure values derived from REMS measurements occur between 4 and 6 am (when *RH* is max), whereas the daytime values show high uncertainties (>100%). This is also valid for other sols not shown in Fig. 6. Therefore, the day-to-night variability in the near-surface water content at Gale crater cannot be analyzed using only REMS data. However, we can shed some light on this variability by comparing the nighttime *PWC* values obtained from REMS (Fig. 7) with the daytime *PWC* values obtained from satellite.

For the first 100 sols of the MSL mission ($L_s \sim 150$–$210°$), Harri et al. (2014a) obtained *PWC* values between 3 and 6 pr-μm using nighttime REMS estimations of the volume mixing ratio (*VMR*) by assuming that the water vapor is uniformly mixed in the nighttime boundary layer. Using nighttime REMS estimations of the water vapor pressure, we obtain *PWC* values at Dingo Gap ranging from 1.2 pr-μm on sols 529–535 ($L_s \sim 86°$) to 2.9 pr-μm on sol 676 ($L_s \sim 154°$) (Fig. 7). Since during the first 100 sols of the mission the near-surface nighttime water vapor pressure (and thus the *VMR*) was roughly between 2 and 3 times higher than during sols 529–676 (Fig. 8), the two estimations of nighttime *PWC* are consistent with each other.

However, daytime estimations of *PWC* from TES climatology at similar latitudes as Gale and for solar longitudes in the range 86–154° (corresponding to the sols shown in Fig. 7) show values of about 10 to 14 pr-μm (Harri et al., 2014a). Similarly, daytime *PWC* estimations from the in situ Mini-TES observations aboard the Opportunity rover (1.95°S) at the same time of the year show values of about 4 to 8 pr-μm (Smith et al., 2006). By comparing these daytime values to the nighttime *PWC* values shown in Fig. 7 (1.2–2.9 pr-μm), a crude day-to-night ratio of about 4 to 6 can be inferred for the near-surface water content at Gale.

A higher day-to-night ratio is obtained at the Phoenix landing site from the analysis of measurements by the TECP instrument and the Surface Stereo Imager (SSI) camera. Using *RH* measurements by the TECP, Rivera-Valentin and Chevrier (2015) have shown typical day-to-night ratios of about 5 early in the mission, with much higher ratios of the order of 10 toward the end of the mission when frost formed every night. Furthermore, the daytime *PWC* value derived by the SSI at the Phoenix landing site was about 30 pr-μm (Tamppari et al., 2010). Since nighttime near-surface water vapor pressure values at the Phoenix landing site at that time were very similar to those at Gale during the first 100 sols (Zent et al., 2012; Harri et al., 2014a), they would have resulted in maximum *PWC* values of about 6 pr-μm (as in Gale for the first 100 sols) assuming a well-mixed atmosphere. This also indicates a day-to-night ratio of about 5 at the Phoenix landing site.

In summary, a day-to-night variability in the near-surface water content at Gale of about 4–6 seems reasonable. During the day, the ground would become a source of water vapor due to desorption and/or sublimation of frost, whereas during the night the ground would become a sink because of adsorption and/or frost deposition (Zent and Quinn, 1997). However, a more comprehensive analysis is needed to quantify the daytime near-surface water content. The Sample Analysis at Mars (SAM) instrument (Mahaffy et al., 2012) has attempted to measure the water vapor pressure (as on the evening of sol 964), but values were below the SAM detection threshold. Measurements between late spring and early summer, when the annual near-surface water content is the highest (Fig. 8) could better constrain the day-to-night variability at Gale crater.

5.3. Impact of surface frost formation on the atmospheric water content

We have estimated values of the order of tenths of μm for the thickness of the frost layer formed at the four locations shown in Fig. 4 between sols 520 and 680. During these sols, the nighttime *PWC* showed values of a few pr-μm (Fig. 7).

On each sol shown in Fig. 7, the ratio between the thickness of the frost layer and the *PWC* can be used to quantify the impact of surface frost formation on the atmospheric water content. This ratio varies from a minimum of 1% on sol 556, to a maximum of 40% on sol 533. These results indicate that either a considerable portion of the *PWC* was deposited on the surface in a few hours, or that substantial horizontal advection brought in moist air from the surroundings, or that the two previous mechanisms were acting together. We believe that a combination of both mechanisms is reasonable. At the Phoenix landing site, a frost layer of about 20 μm thick was estimated using satellite measurements (Cull et al., 2010) when the daytime *PWC* was about 30 pr-μm (Tamppari et al., 2010). It has been suggested that regional atmospheric circulations are inhibited at Gale crater (Moores et al., 2015) and therefore water vapor transport does not cause significant variability in the atmospheric water vapor content. Since the terrains on which frost likely formed (Fig. 4) were colder than their surroundings due to their low thermal inertia, they could have acted as a cold trap of water vapor, locally enhancing its transport.

6. Summary and conclusions

We provide indirect evidence for the formation of frost at the surface of Gale crater by analyzing simultaneous measurements of relative humidity and ground temperature with the highest confidence during the first 1000 sols of the MSL mission. We find that the most likely frost events occurred at four different locations: Dingo Gap megaripple during sols 529–535, an unnamed place during sols 554–560, Kimberley during sols 609–617, and an unnamed place during sols 673–676, corresponding to the most humid and coldest time of the year (from late fall to early winter; Figs. 1 and 2). At these four locations, the terrain features thermal inertia of ~200 SI units, a value much lower than that obtained from satellite measurements at the landing ellipse of 365 ± 50 SI units. This is important because terrains with exceptionally low *I* values, consistent with fine-grained and loosely packed material (Fig. 4), favor the formation of frost by producing lower daily minimum ground temperatures than terrains with higher thermal inertia values.

We select sols 531, 557, 612 and 676 to analyze the environmental conditions that most likely resulted in the formation of frost. The ground temperature was below the frost point with the highest confidence between 4 and 6 am on sol 531, between 4 and 5 am on sols 557 and 612, and only at 5 am on sol 676 (Fig. 5), indicating that frost is most likely to form during these time periods. Furthermore, the water vapor pressure decreased during these periods on each sol (Fig. 6), consistent with loss of water vapor by frost formation.

We calculate a lower-bound estimate for the thickness of the frost layer developed at these four locations of the order of tenths of μm, with the precipitable water content showing values of a few pr-μm (Fig. 7). These results suggest that either a considerable portion of the *PWC* was deposited on the surface in a few hours, or that the terrain at these four locations was acting as a cold trap, bringing in moist air from the surroundings. We believe that a combination of both mechanisms is plausible.

Since water vapor pressure values derived from REMS measurements present high uncertainties during the daytime (Fig. 6), the day-to-night variability in the near-surface water content at Gale cannot be analyzed using only REMS products. By comparing the nighttime *PWC* values obtained from REMS (Fig. 7) with the daytime *PWC* values obtained from satellite, we estimate a crude day-to-night ratio of the near-surface water vapor pressure at Gale of about 4–6.

Frost formation at Gale crater has important implications for the local ground–atmosphere interaction, the geochemistry and the geologic nature of the surface and near sub-surface. In addition, it could explain the ubiquitous hydration signature observed from orbit as well as the formation of the hydrated amorphous component documented by the Curiosity payload in the martian soil.

Acknowledgments

This research is supported by JPL grant number 1449038. The author A. Vicente-Retortillo wishes to acknowledge the Spanish Ministry of Economy and Competitiveness (MINECO) for the granted FPI fellowship (BES-2012-059241).

Appendix A

A.1. REMS GTS measurements: uncertainties

The GTS measurements and their specifications can be found in the NASA Planetary Data System (PDS). In this study we only use GTS measurements with the ASIC power supply in range, the highest recalibration quality, and with no shadows in the GTS FOV. By averaging these measurements over an interval of 5 min (nominal measuring strategy of the GTS), we produce high quality hourly values of ground temperature ($\overline{T_g}$).

In order to calculate the absolute uncertainty σ_{Tg} of the mean $\overline{T_g}$, we use REMS GTS random uncertainties and systematic long-term uncertainties (sys_{error}). The former represent the standard deviation of the mean while the latter represent the absolute systematic uncertainty of the sensor, which includes the impact of calibration errors and the sensor degradation on the accuracy of the GTS. Since the random and systematic uncertainties arise from adding up several uncorrelated errors of different origin and nature (thermal and electrical), we add them quadratically to calculate the absolute uncertainty of $\overline{T_g}$ as

$$\sigma_{Tg} = \sqrt{\left(\frac{\sigma'_{Tg}}{\sqrt{N}}\right)^2 + \overline{(sys_{error})}^2}, \tag{A.1}$$

where the first term on the right accounts for the random uncertainty and the second for the systematic uncertainty. Specifically, the random uncertainty is represented by the standard deviation of the mean, which is calculated from the standard deviation (σ'_{Tg}) of N GTS measurements averaged over a 5 min interval. Finally, the systematic uncertainty is calculated as the mean of the absolute systematic error of each GTS measurement over a 5 min interval.

A.2. REMS RHS measurements: uncertainties

The REMS/RHS products that can be found in the NASA PDS are the relative humidity (RH), its uncertainty (ΔRH), and the temperature (T_{RH}). Using these three quantities, we show next how to calculate the water vapor pressure at 1.6 m ($e1.6m$) and its uncertainty ($\delta e1.6m$), as well as the frost point (T_f) and its uncertainty ΔT_f.

The uncertainty in RH and in T_{RH} is given by

$$\Delta RH\ (\%) = \begin{cases} 2, & T_{RH} > 243\ \text{K} \\ 10{,}203\ \text{K} \le T_{RH} \le 243\ \text{K}, \\ 20, & T_{RH} < 203\ \text{K} \end{cases} \tag{A.2}$$

$$\Delta T_{RH}\ (\text{K}) = 0.2 \quad \forall T_{RH}. \tag{A.3}$$

By definition, $e1.6m$ can be obtained as

$$e1.6m = RH \times e_s(T_{RH}), \tag{A.4}$$

where e_s is the saturation vapor pressure over ice expressed as

$$e_s = a e^{\frac{b(T-c)}{(T+d)}}, \tag{A.5}$$

where $a = 611.35$ Pa, $b = 22.45$, $c = 273.16$ K and $d = 0.32$ K (Savijärvi et al., 2015). By substituting Eq. (5) into Eq. (4) and taking differentials on Eq. (4), we obtain the uncertainty in the water vapor pressure as

$$\delta e \simeq e\left(\frac{\Delta RH}{RH} + bc\frac{\Delta T_{RH}}{T_{RH}^2}\right). \tag{A.6}$$

The frost point is defined as the temperature at which the saturation vapor pressure over ice is equal to the atmospheric water vapor pressure. Therefore, T_f can be obtained from Eq. (5) by rearranging terms as

$$T_f = \frac{c + zd}{1 - z}, \tag{A.7}$$

where

$$z = \frac{1}{b}\ln\frac{e}{a}. \tag{A.8}$$

Taking differentials on Eq. (A.7), we finally obtain

$$\Delta T_f = \frac{T_f}{b}\frac{\delta e}{e}\left(\frac{d}{c + zd} + \frac{1}{1 - z}\right). \tag{A.9}$$

Eqs. (3), (4), (6)–(9) can be used to calculate $e1.6m$, $\delta e1.6m$, T_f and ΔT_f from the RHS products RH, ΔRH and T_{RH} found in the NASA PDS. We note that very similar values of $e1.6m$, $\delta e1.6m$, T_f and ΔT_f have been obtained using the Goff–Gratch relation for e_s instead of the Buck relation shown in Eq. (5).

References

Audouard, J., et al., 2014. Water in the martian regolith from OMEGA/Mars Express. J. Geophys. Res.: Planets 119 (8), 1969–1989 (2014).

Christensen, P.R., et al., 2001. Mars Global Surveyor Thermal Emission Spectrometer experiment: Investigation description and surface science results. J. Geophys. Res. 106, 23823–23871. doi:10.1029/2000JE001370.

Clark, B.C., et al., 1982. Chemical composition of martian fines. J. Geophys. Res. 87, 10059–10067.

Cull, S., et al., 2010. Seasonal ice cycle at the Mars Phoenix landing site: 2. Post-landing CRISM and ground observations. J. Geophys. Res. 115 (E5), E00E19. doi:10.1029/2009JE003410.

Fergason, R.L., et al., 2012. Surface properties of the Mars Science Laboratory candidate landing sites: Characterization from orbit and predictions. Space Sci. Rev. 170 (1–4), 739–773.

Fischer, E., et al., 2014. Experimental evidence for the formation of liquid saline water on Mars. Geophys. Res. Lett. 41, 4456–4462. doi:10.1002/2014GL060302.

Gómez-Elvira, J., et al., 2012. REMS: The environmental sensor suite for the Mars Science Laboratory rover. Space Sci. Rev. 170 (1–4), 583–640.
Gómez-Elvira, J., et al., 2014. Curiosity's Rover Environmental Monitoring Station: Overview of the first 100 sols. J. Geophys. Res.: Planets 119 (7), 1680–1688.
Grotzinger, J.P., et al., 2012. Surface properties of the Mars Science Laboratory candidate landing sites: Characterization from orbit and predictions. Space Sci. Rev. 170 (1–4), 739–773.
Hamilton, V.E., et al., 2014. Observations and preliminary science results from the first 100 sols of MSL Rover Environmental Station ground temperature sensor measurements at Gale Crater. J. Geophys. Res.: Planets 119, 745–770. doi:10.1002/2013JE004520.
Harri, A.-M., et al., 2014. Mars Science Laboratory relative humidity observations: Initial results. J. Geophys. Res.: Planets 119 (9), 2132–2147.
Harri, A.M., et al., 2014. Pressure observations by the Curiosity rover: Initial results. J. Geophys. Res.: Planets 119 (1), 82–92.
Jakosky, B.M., Christensen, P.R., 1986. Global duricrust on Mars: Analysis of remote sensing data. J. Geophys. Res. 91, 3547–3559.
Jakosky, B.M., et al., 1997. The Mars water cycle: Determining the role of exchange with the regolith. Icarus 130 (1), 87–95.
Jones, K.L., et al., 1979. One Mars year: Viking lander imaging observations. Science 204 (4395), 799–806.
Landis, G.A., 2007. Observation of frost at the equator of Mars by the Opportunity rover. Lunar Planet. Sci. 38, 2423 (abstracts).
Leshin, L.A., et al., 2013. Volatile, isotope, and organic analysis of martian fines with the Mars Curiosity rover. Science 341 (6153), 1238937-1–1238937-9. doi:10.1126/science.1238937.
Mahaffy, P.R., et al., 2012. The sample analysis at Mars investigation and instrument suite. Space Sci. Rev. 1–78.
Martínez, G.M., Renno, N.O., 2013. Water and brines on Mars: Current evidence and implications for MSL. Space Sci. Rev. 175 (1–4), 29–51.
Martínez, G.M., et al., 2014. Surface energy budget and thermal inertia at Gale crater: Calculations from ground-based measurements. J. Geophys. Res.: Planets 119 (8), 1822–1838.
Martín-Torres, F.J., et al., 2015. Transient liquid water and water activity at Gale crater on Mars. Nat. Geosci. 8, 357–361.
Maurice, S., et al., 2012. The ChemCam instrument suite on the Mars Science Laboratory (MSL) rover: Science objectives and mast unit description. Space Sci. Rev. 170 (1–4), 95–166.
Mellon, M.T., Feldman, W.C., Prettyman, T.H., 2004. The presence and stability of ground ice in the southern hemisphere of Mars. Icarus 169 (2), 324–340.
Meslin, P.-Y., et al., 2013. Soil diversity and hydration as observed by ChemCam at Gale crater, Mars. Science 341 (6153), 1238670. doi:10.1126/science.1238670.
Mitrofanov, I.G., et al., 2012. Dynamic Albedo of Neutrons (DAN) experiment onboard NASA's Mars Science Laboratory. Space Sci. Rev. 170 (1–4), 559–582.
Mitrofanov, I.G., et al., 2014. Water and chlorine content in the martian soil along the first 1900 m of the Curiosity rover traverse as estimated by the DAN instrument. J. Geophys. Res.: Planets 119 (7), 1579–1596.
Möhlmann, T.F., 2008. The influence of van der Waals forces on the state of water in the shallow subsurface of Mars. Icarus 195 (1), 131–139.
Moores, J.E., et al., 2011. Observations of near-surface fog at the Phoenix Mars landing site. Geophys. Res. Lett. 38 (4), L04203. doi:10.1029/2010GL046315.
Moores, J.E., et al., 2015. Observational evidence of a suppressed planetary boundary layer in northern Gale crater, Mars as seen by the Navcam instrument onboard the Mars Science Laboratory rover. Icarus 249, 129–142.
Putzig, N.E., et al., 2005. Global thermal inertia and surface properties of Mars from the MGS mapping mission. Icarus 173, 325–341.
Rieder, R., et al., 1997. The chemical composition of martian soil and rocks returned by the Mobile Alpha Proton X-ray Spectrometer: Preliminary results from the X-ray mode. Science 278, 1771–1774.
Rieder, R., et al., 2004. Chemistry of rocks and soils at Meridiani Planum from the alpha particle X-ray spectrometer. Science 306, 1746–1749.
Rivera-Valentin, E.G., Chevrier, V.F., 2015. Revisiting the Phoenix TECP data: Implications for regolith control of near-surface humidity on Mars. Icarus 253, 156–158.
Savijärvi, H., 1995. Mars boundary layer modeling: Diurnal moisture cycle and soil properties at the Viking Lander 1 site. Icarus 117 (1), 120–127.
Savijärvi, H., 1999. A model study of the atmospheric boundary layer in the Mars Pathfinder lander conditions. Q. J. R. Meteorol. Soc. 125 (554), 483–493.
Savijärvi, H., 2012. The convective boundary layer on Mars: Some 1-D simulation results. Icarus 221 (2), 617–623.
Savijärvi, H., Määttänen, A., 2010. Boundary-layer simulations for the Mars Phoenix lander site. Q. J. R. Meteorol. Soc. 136 (651), 1497–1505.
Savijärvi, H.I., Harri, A.M., Kemppinen, O., 2015. Mars Science Laboratory diurnal moisture observations and column simulations. J. Geophys. Res.: Planets 120, 1011–1021. doi:10.1002/2014JE004732.
Schorghofer, N., Aharonson, O., 2005. Stability and exchange of subsurface ice on Mars. J. Geophys. Res. 110, E05003. doi:10.1029/2004JE002350.
Schröder, S., et al., 2015. Hydrogen detection with ChemCam at Gale crater. Icarus 249, 43–61.
Sebastián, E.C., et al., 2010. The Rover Environmental Monitoring Station Ground Temperature Sensor: A pyrometer for measuring ground temperature on Mars. Sensors 10 (10), 9211–9231.
Smith, M.D., et al., 2006. One martian year of atmospheric observations using MER Mini-TES. J. Geophys. Res. 111 (E12), E12S13. doi:10.1029/2006JE002770.
Smith, P.H., et al., 2009. H_2O at the Phoenix landing site. Science 325 (5936), 58–61.
Sullivan, R., Zimbelman, J., 2015. Megaripples and their sedimentary deposits on Earth and Mars. Lunar Planet. Sci. XLVI, 2762.
Sullivan, R., et al., 2005. Aeolian processes at the Mars Exploration Rover Meridiani Planum landing site. Nature 436. doi:10.1038/nature03641.
Sullivan, R. et al., 2014. Transverse aeolian ridges (TARs) as megaripples: Rover encounters at Meridiani Planum, Gusev and Gale. Lunar Planet. Sci. XLVI, 1424.
Tamppari, L.K., et al., 2010. Phoenix and MRO coordinated atmospheric measurements. J. Geophys. Res. 115 (E5), E00E17. doi:10.1029/2009JE003415.
Wall, S.D., 1981. Analysis of condensates formed at the Viking 2 Lander site: The first winter. Icarus 47 (2), 173–183.
Whiteway, J.A., et al., 2009. Mars water-ice clouds and precipitation. Science 325 (5936), 68–70.
Zent, A.P., Quinn, R.C., 1997. Measurement of H_2O adsorption under Mars-like conditions: Effects of adsorbent heterogeneity. J. Geophys. Res.: Planets (1991–2012) 102 (E4), 9085–9095.
Zent, A.P. et al., 2012. A revised calibration function for the TECP humidity sensor of the Phoenix mission. Lunar Planet. Sci. 43, 2846.